Journal of Materials Chemistry A

ROYAL SOCIETY OF CHEMISTRY

PAPER

View Article Online
View Journal | View Issue

Cite this: J. Mater. Chem. A, 2022, 10, 209

Phase stability and sodium-vacancy orderings in a NaSICON electrode†

Ziliang Wang,[a] Sunkyu Park,[bcd] Zeyu Deng,[a] Dany Carlier,[cd] Jean-Noël Chotard,*[bd] Laurence Croguennec,[cd] Gopalakrishnan Sai Gautam,[e] Anthony K. Cheetham,[af] Christian Masquelier[bd] and Pieremanuele Canepa*[ag]

Received 28th October 2021
Accepted 2nd December 2021

DOI: 10.1039/d1ta09249a

rsc.li/materials-a

We elucidate the complex thermodynamics of sodium (Na) intercalation into the sodium super-ionic conductor (NaSICON)-type electrode, $Na_xV_2(PO_4)_3$, for promising Na-ion batteries with high-power density. This is the first report of a computational temperature-composition phase diagram of the NaSICON-type electrode $Na_xV_2(PO_4)_3$. Based on our computational data, we identify a thermodynamically stable phase with a composition of $Na_2V_2(PO_4)_3$ and describe its structural features. We also identify another metastable configuration that can occur at room temperature, namely $Na_{3.5}V_2(PO_4)_3$. We unveil the crystal-structure and the electronic-structure origins of the ground-state compositions associated with specific Na/vacancy arrangements, which are driven by charge orderings on the vanadium sites. These results are significant for the optimization of high-energy and power density electrodes for sustainable Na-ion batteries.

Introduction

The urgent demands for the next-generation of clean energy technologies put increasing pressure on researchers to develop innovative materials and devices. Due to the high energy densities and desirable electrochemical cycling performance, lithium-ion batteries (LIBs) have been extensively investigated for their use in portable devices and vehicular transportation.[1] However, the expanding LIB industry may soon be limited by the availability of lithium and specific transition metals (mostly cobalt and nickel) that are only accessible in limited geographic locations, often with socio-political instabilities and/or restrictions by government policies.[2,3] Given the widespread abundance of Na-metal resources, sodium (Na)-ion batteries (NIBs) appear to be an ideal alternative of LIBs particularly for stationary applications.[4–8]

The Natrium Super Ionic CONductor (NaSICON),[9,10] relying on a robust covalent framework and tunable electrochemical properties,[11,12] has been actively investigated as alternative electrode materials to the transition-metal layered oxides for NIBs.[13,14] The high-voltages delivered by specific NaSICON compositions require a careful selection of liquid electrolytes[15] and an understanding of the solid-electrolyte interphase.[16–18] NaSICON-type solid electrolytes have also been applied to NIBs due to their prominent Na ionic conductivity.[19]

The NaSICON-based vanadium phosphate, in the $Na_3V_2(PO_4)_3$ (N_3VP) phase and its electrochemically-derived phases, $Na_1V_2(PO_4)_3$ (N_1VP) and $Na_4V_2(PO_4)_3$ (N_4VP) have received significant attention as a promising positive electrode material for NIBs.[11,12,14,20,21] Throughout this manuscript, we use N_xVP to indicate $Na_xV_2(PO_4)_3$ at a Na composition, x. Several investigations have been conducted to improve the electrochemical performance of N_xVP (energy density $\sim$ 370 W h kg^{-1} theoretically cycling at N_3VP-N_1VP), for example, by mixing V partially with other transition metals.[11,21–23] Specifically, in the composition range $1 \leq x \leq 3$, N_xVP intercalates Na at a relatively high voltage ($\sim$3.4 V *vs.* Na/Na$^+$)[20] and displays a limited volume change upon reversible Na insertion (*i.e.*, $\sim$234.41 Å^3 f.u.$^{-1}$ in N_3VP and $\sim$219.50 Å^3 f.u.$^{-1}$ in N_1VP). In contrast, reversible Na (de)intercalation in layered transition metal oxides typically provides lower voltages than NaSICON electrodes, as well as volume changes that may curb their use in practical NIBs.[6,24–26]

As shown in Fig. 1(a), the framework of N_xVP is built around a common structural motif—the "lantern unit"—consisting of

[a]Department of Materials Science and Engineering, National University of Singapore, 9 Engineering Drive 1, 117575, Singapore. E-mail: pcanepa@nus.edu.sg
[b]Laboratoire de Réactivité et de Chimie des Solides (LRCS), CNRS UMR 7314, Université de Picardie Jules Verne, 80039 Amiens Cedex, France. E-mail: jean-noel.chotard@u-picardie.fr
[c]CNRS, Univ. Bordeaux, Bordeaux INP, ICMCB, UMR CNRS 5026, Pessac, F-33600, France
[d]RS2E, Réseau Français sur le Stockage Electrochimique de l'Energie, FR CNRS 3459, F-80039 Amiens Cedex 1, France
[e]Department of Materials Engineering, Indian Institute of Science, Bengaluru, Karnataka, 560012, India
[f]Materials Department and Materials Research Laboratory, University of California, Santa Barbara, California 93106, USA
[g]Department of Chemical and Biomolecular Engineering, National University of Singapore, 4 Engineering Drive 4, 117585 Singapore, Singapore

† Electronic supplementary information (ESI) available. See DOI: 10.1039/d1ta09249a

two VO_6 octahedra sharing corners with three PO_4 tetrahedra moieties.[9–11,27] In principle, the NaSICON structure can host up to 4 Na ions to form N_4VP[6,28,29] with a rhombohedral ($R\bar{3}c$) structure.[30–32] In practice, the Na^+ extraction/insertion is limited to only 3 ions (per two vanadiums) in the range N_1VP–N_4VP. It is impossible to extract the 4th Na ion from N_1VP although the V(IV)/V(V) redox couple is theoretically accessible.[21,33,34] In the $R\bar{3}c$ N_xVP, two distinct Na sites exist: Na(1) and Na(2). The Na(1) site is 6-coordinated and sandwiched between 2 VO_6 octahedra, whereas Na(2) (yellow or black-outlined circles in Fig. 1(a)) occupies the "interstitials" formed by PO_4 units. In N_4VP, both Na(1) and Na(2) sites are fully occupied. A partial occupancy of Na in the Na(2) sites (such as in N_3VP, where sodium ordering occurs) can further reduce the $R\bar{3}c$ symmetry, resulting in a monoclinic structure.[31]

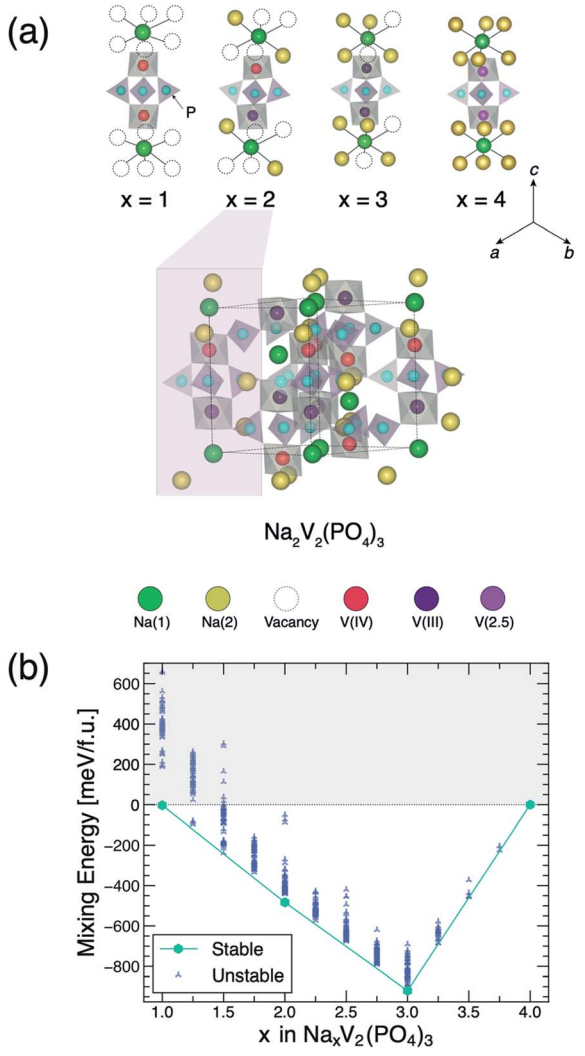

Fig. 1 Phase diagram at 0 K and stable orderings of N_xVP identified by DFT. Panel (a) depicts the local environments of the stable Na/vacancy orderings of panel (b) in the format of "lantern units". Na(1) and Na(2) sites, vanadium species, *i.e.*, V(IV), V(III), V(2.5), and P sites are identified with green, yellow, red, violet, pink, and light blue circles, respectively. A zoom out of the N_2VP structure is shown emphasizing its "lantern unit" in the pink box. Vacancy Na^+ sites are represented by open circles. Charges on the vanadium sites are derived from the integrated magnetic moments, as calculated by DFT. Panel (b) shows the mixing energies for all Na/vacancy orderings *vs.* Na content (x) in N_xVP. The solid line (aqua) shows the convex hull envelope constructed by the most stable phases, identified by the aqua hexagons, *i.e.* N_1VP ($R\bar{3}c$), N_2VP ($P\bar{1}$), N_3VP (monoclinic Cc), and N_4VP ($R\bar{3}c$).

While these studies are certainly important, the community still does not fully understand the sheer complexity of the mechanism of Na extraction from N_3VP, itself (during the first charge of the battery), which must be clarified to make N_xVP a successful commercial electrode material. Chotard *et al.* identified specific Na/vacancy orderings in N_3VP at different temperatures using synchrotron X-ray diffraction.[31] Upon reversible Na (de)intercalation, such orderings may be facilitated by charge ordering on the vanadium sites, though the mechanism is far from being fully understood.[20,21,31] These studies suggest that a complex interplay of Na/vacancy orderings, together with the variation in the electronic structure of vanadium, drives the formation of specific N_xVP phases during Na (de)intercalation, which is the focus of this work.

Here, we reveal the driving forces behind the phase transitions of the N_xVP framework, which occur as temperature and Na composition ($1 \leq x \leq 4$) are varied, using a multiscale model based on density functional theory (DFT) and grand-canonical Monte Carlo (gcMC) simulations. We analyze the relevant Na site occupancies, intercalation voltages, and entropies of Na intercalation as a function of temperature. Importantly, our theoretical study reveals the Na/vacancy ordering in the thermodynamically stable phase, N_2VP, whose signature has been previously reported.[35] Recent *operando* measurements have also confirmed the existence and the structural features of this intermediate N_2VP phase.[36] Notably, this is the first instance where the compositional phase diagram of a NaSICON electrode is derived from first principles. The results of our work shed light on the complexity of Na (de)insertion in NaSICON electrodes for novel NIBs.

Results

To understand the process of sodium extraction/intercalation in the N_xVP structure, we use DFT calculations to parameterize a cluster expansion Hamiltonian, which in turn is used for energy evaluations within gcMC simulations, resulting in the estimation of thermodynamic properties as a function of temperature (and composition).[37–39] We described the exchange and correlation term in DFT using the strongly constrained and appropriately normed (SCAN) *meta*-generalized gradient approximation (*meta*-GGA) functional.[40] Additionally, we added a Hubbard U correction of 1.0 eV on all V atoms (*i.e.*, SCAN + U) to appropriately localize the 3d electrons and reduce the spurious self-interaction errors.[41,42] Details on these methodologies are provided in the Methodology and ESI.†[41,42]

Fig. 1(b) shows the DFT mixing energies of the N_xVP system at 0 K, referenced to the N_1VP and N_4VP compositions, which elucidate the thermodynamic driving forces for Na (de)intercalation. The mixing energies in Fig. 1(b) do not include entropy contributions. We enumerated all the different Na/vacancy configurations within 2 × 2 × 1 supercells (with 168 atoms) of

the primitive rhombohedral cell (2 f.u. with 21 atoms per f.u.) and sampled Na compositions with a step size of $x = 0.25$ (see details in ESI†). The envelope of points minimizing the mixing energy—the convex hull—comprises the stable Na/vacancy orderings (aqua hexagons in Fig. 1(b)) at 0 K, namely, $x = 1$, 2, 3, and 4 in N_xVP. Other Na/vacancy configurations (blue markers in Fig. 1(b)) are metastable (or unstable) and will decompose or phase separate into nearby stable phases at 0 K. Several metastable configurations are observed to be close to the convex hull, such as $N_{1.5}VP$, $N_{2.5}VP$ and $N_{3.5}VP$ (with energy ~4.4 meV f.u.$^{-1}$, ~24.5 meV f.u.$^{-1}$, and ~8.0 meV f.u.$^{-1}$ above the convex hull, respectively).

Our calculations indicate that the stable "end-member" compositions, namely N_1VP and N_4VP adopt the $R\bar{3}c$ rhombohedral space group, in agreement with existing X-ray diffraction experiments.[21] We find the monoclinic distortion of N_3VP (Cc), which is also a global minima (~920 meV f.u.$^{-1}$) in the convex hull of Fig. 1(b), in agreement with experimental observation.[31] Remarkably, our DFT calculations discover a previously uncharted, thermodynamically stable Na-vacancy configuration at $x = 2$, *i.e.*, N_2VP (Fig. 1(a)). In the ground state structure of N_2VP, the Na ions and vacancies are initialized in a monoclinic setting ($C2/c$), with geometry optimization by DFT further distorting the structure into a triclinic ($P\bar{1}$) symmetry (see further discussions below).

Fig. 1(a) shows the "lantern units" of the computed ground states of N_xVP at $x = 1$, 2, 3, and 4, emphasizing the Na/vacancy orderings in relation to the charge orderings on the vanadium(v) sites. The integration of the DFT-calculated spin density on each V site provides magnetic moments, which are directly related to the oxidation states of the V atoms (see Table S4 of ESI†). Table S3 of ESI† lists the V–O bond lengths for all the N_xVP ground states, which is particularly useful for identifying V(IV) sites, as demonstrated by the existence of shorter (~1.82 Å) V(IV)–O bonds. In N_1VP and N_3VP, only one type of V site is observed, *i.e.*, V(IV) and V(III), respectively, which fulfils the charge-neutrality of the corresponding structures. On the other hand, the ground state configuration at N_2VP exhibits "lantern units" containing one V(III) and one V(IV).

In N_4VP, we could not distinguish the two V sites (light violet circles in Fig. 1(a)), as this composition shows metallic behaviour, which is discussed in the density of states (DOS) and the band structures of Fig. S1 and S3,† respectively. The metallic behaviour of N_4VP results in fractional oxidation states of V (~2.5), as extracted from the calculated magnetic moments (Table S4†), and in agreement with previous theoretical calculations.[12] The analysis of the N_4VP band structure in Fig. S3† suggests that only four bands contribute actively at the Fermi energy, which indicates that the predicted metallic behaviour may be an artifact of DFT. In fact, prior hybrid DFT calculations predicted N_4VP as a semiconductor with a small band gap of ~0.3 eV.[12]

The projected DOS in Fig. S1(a) to (d)† exhibit predominant V 3d states at the valence band edges and/or near the Fermi energy. As Na concentration (x) increases in N_xVP from 1 to 4, the V 3d states are shifted to higher energies, first reducing and eventually closing the band gap at N_4VP. The decreasing band gap with the reduced vanadium oxidation state (and increasing Na content) in N_xVP also follows the trends of other compounds containing V,[43–45] where compounds with V(IV) show less tendency to undergo a semiconductor-to-metal transition near room temperature than compounds containing V(III). Hence, the qualitative trend of our band gap predictions is robust.

The appreciable increase in band gap at N_3VP (~1.4 eV), with respect to N_1VP (~0.7 eV) or N_2VP (~0.3 eV) is attributed to the monoclinic distortion, which stabilizes the N_3VP structure.[12] As shown by the spin-polarized DOS projected onto the V 3d orbitals of Fig. S2,† the valence band edge (VBE) of N_3VP is mainly dominated by vanadium orbitals with t_{2g} character, whereas the conduction band edge (CBE) consists of both V t_{2g} and e_g orbitals. Note that the monoclinic distortion in N_3VP is largely driven by electrostatic interactions, which is signified by Na fully occupying the Na(1) sites while selectively occupying a subset of Na(2) sites (see Fig. 1(a)). Thus, the increase in band gap of N_3VP can be attributed to the electrostatic interactions within the monoclinic structure, which preferably stabilize the V t_{2g} states of the VBE relative to the t_{2g} and e_g states comprising the CBE.

The knowledge of the temperature *vs.* Na composition (T *vs.* x) phase diagram is also of immediate importance for understanding the extraction/intercalation of Na^+ from/into N_xVP and for identifying commonalities in the structure–property relationships of other NaSICON electrodes or electrolytes. The temperature *vs.* composition phase diagram in Fig. 2 is derived from gcMC simulations, with supercells containing more than 172 032 atoms and ranged over 32 768 000–327 680 000 Monte Carlo steps for all T and x samples combined. The cluster

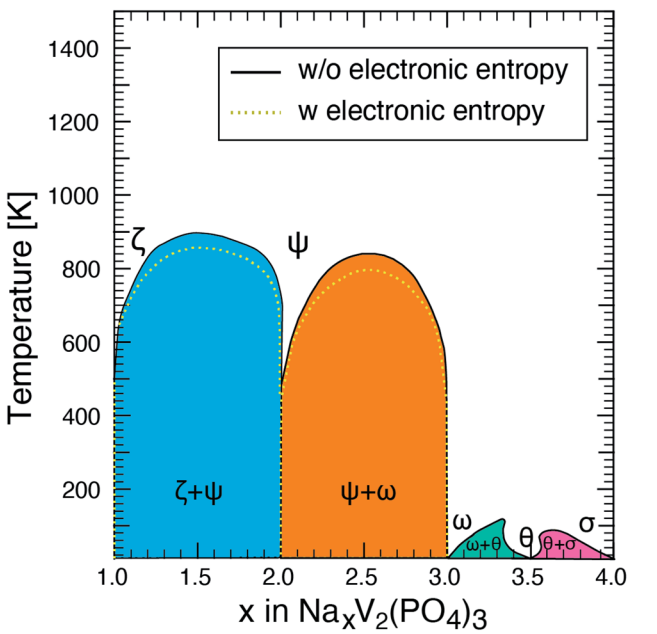

Fig. 2 Computed phase diagram of N_xVP at variable Na contents (x) and temperatures (T) from gcMC simulations. Solid and dashed lines show the phase boundaries. Dashed yellow lines in the region $1 \leq x \leq 3$ represent phase boundaries obtained by introducing electronic entropy gained by mixing of the V(III) with V(IV) oxidation states.

expansion Hamiltonian, used for the energy evaluations in gcMC was fitted on DFT-calculated mixing energies of ~849 Na/vacancy configurations (see ESI† for more details).

Fig. 2 exhibits five single-phase regions, namely, ζ, ψ, ω, θ and σ, which correspond largely to Na compositions of $x = 1$, 2, 3, 3.5, and 4, respectively. The two-phase regions in Fig. 2 are indicated by the coloured domes, with solid black and dashed yellow lines indicating their boundaries without and with electronic entropy contributions, respectively (see discussion below). Specifically, the two-phase regions in Fig. 2 are: $\zeta + \psi$ below 890 K and at $1 < x < 2$ (light-blue dome), $\psi + \omega$ (orange dome at $2 < x < 3$, $T < 840$ K), $\omega + \theta$ (aqua dome at $3 < x < 3.5$, $T < 120$ K), and $\theta + \sigma$ (pink dome at $3.5 < x < 4$, $T < 100$ K). Notably, the $\zeta + \psi$, and $\psi + \omega$ two-phase regions are stable over a wide-range of temperatures (0–800 K) compared to the other two-phase regions. The θ phase detected by gcMC appears to be stable only above 10 K (not visible in Fig. 2), and is metastable at 0 K (Fig. 1(b)). Thus, θ decomposes to form a two-phase $\omega + \sigma$ mixture, *via* an eutectoid reaction at ~10 K and $x = 3.5$.

One remarkable finding from this phase diagram is the previously unidentified single-phase ($P\bar{1}$), ψ, at $x = 2$, which exists as a line compound up to $T < 480$ K. The solubility of excess Na in the ψ phase increases significantly at higher temperatures ($T > 480$ K), eventually leading to the closing of the $\psi + \omega$ miscibility gap at ~850 K. The ψ phase also exhibits Na-vacancy solubility at high temperatures ($T > 630$ K), resulting in the closing of the $\zeta + \psi$ two-phase region at T ~890 K. In general, we note that the N_xVP phase diagram appears qualitatively similar to that of the NaSICON solid electrolyte, $Na_{1+x}Zr_2Si_xP_{3-x}O_{12}$,[27] which exhibits three distinct single-phase regions.

We assign oxidation states of V(III) and V(IV) to the vanadium atoms in N_3VP and N_1VP, respectively, for our 0 K calculations based on integrated magnetic moments. However, at intermediate Na compositions ($1 < x < 3$), the charges V(III) and V(IV) may disorder across the available V sites, owing to thermally-activated electronic or polaronic hops,[46,47] especially at higher temperatures. Therefore, we introduce the effect of electronic entropy, $\Delta S_{electronic}$, as induced by possible disordering (or accessing multiple configurations) of V(III)/V(IV) charges *via* the ideal solution model (eqn (1)):

$$\Delta S_{electronic} = -k_B N[(m ln(m) + (1 - m)\ln(1 - m))] \quad (1)$$

where, k_B is the Boltzmann constant, N is the number of vanadium sites per primitive cell (*i.e.*, 4 sites per 2 f.u.), and m is the mole fraction of V(III) oxidation states ($m = 0$ at N_1VP and $m = 1$ at N_3VP). Note that the ideal solution model provides an upper bound to the magnitude of $\Delta S_{electronic}$.

The inclusion of electronic entropy modifies the phase boundaries of the $\zeta + \psi$ and $\psi + \omega$ two-phase regions (see dashed yellow lines in Fig. 2). Specifically, including electronic entropy lowers the critical temperatures of both the two-phase regions (*i.e.*, the highest temperature up to which a two-phase region exists) by ~50 K. The electronic entropy also increases the Na solubility in ψ phase, characterized by an increase in the stability range of the ψ phase at higher Na contents for a given temperature.

We also analysed the occupancy of Na(1) and Na(2) sites, obtained from the gcMC simulations, across the Na composition range ($1 \leq x \leq 4$) at three specific temperatures: 263 K (Fig. 3(a)), 473 K (Fig. 3(b)) and 920 K (Fig. 3(c)), and compared with available experimental data at 263 K and 473 K,[31] respectively. The 920 K is selected to represent the Na occupancy in the solid solution region where all two-phase regions cease to exist (Fig. 2). For all Na compositions in N_xVP and at all temperatures considered, the occupation of Na(2) increases monotonically from 0 to 1 upon increasing x (see pink lines and dots in Fig. 3). In contrast, the Na(1) site remains fully occupied at 263 K (green lines and dots) across the whole composition range. Our predictions at 263 K are in excellent agreement with the experimental value from synchrotron X-ray experiments by Chotard *et al.*[31] At higher temperatures (473 K and 920 K), Na(1) is fully occupied only for $1 \leq x \leq 3$, while its occupancy decreases between N_3VP and $N_{3.1}VP$ and subsequently increases again from $N_{3.1}VP$ to N_4VP. Remarkably, at 473 K and 920 K and $x > 3.05$, both Na(1) and Na(2) sites show similar occupancies, indicating significant disorder across both Na sites, in line with the observed single-phase regions ($\omega/\theta/\sigma$) of Fig. 2.

Our simulated Na occupancy of the Na(2) site at the N_3VP composition at 473 K accurately reproduces the experimental data of ref. 31. Although we overestimate the Na(1) occupancy (~1) compared to experiment (~0.75) at N_3VP,[31] we predict a sharp decrease of the Na(1) occupation at x slightly above 3

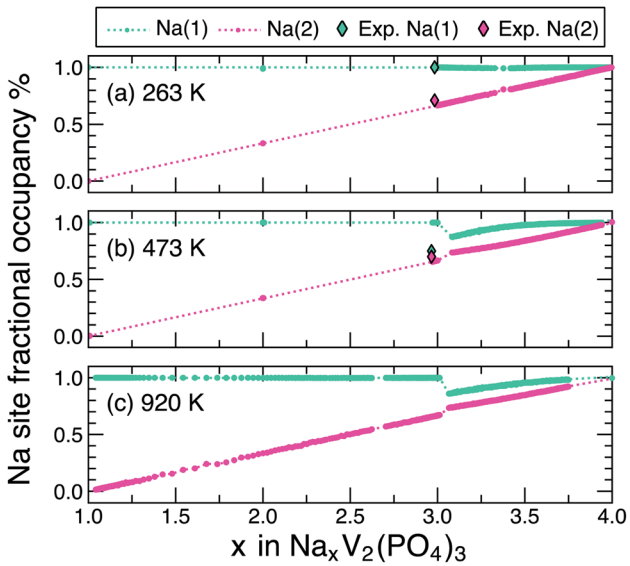

Fig. 3 Na occupancies of Na(1) sites (green) and Na(2) sites (pink) in N_xVP at 263 K (panel (a)), 473 K (panel (b)), and 920 K (panel (c)) *vs.* Na composition as extracted from gcMC simulations. Coloured dots represent data in the single-phase regions of the phase diagram of Fig. 2. The dashed lines denote the Na(1)/Na(2) distributions within the two-phase regions and are derived by interpolation between gcMC-simulated fractional occupations of the bounding single-phase regions. The experimental occupancies of Na(1) and Na(2) at 263 K and 473 K (ref. 31) are represented by green and pink diamond, respectively.

(*e.g.*, $x = 3.05$), which is in better agreement with the experimental occupancy of Na(1).[27] This suggests that the experimental samples intended as N_3VP may be slightly off-stoichiometric. In any case, the decrease of Na(1) occupancy at x marginally greater than 3, especially at higher temperatures (473 K and 920 K) is likely because of a higher gain in configurational entropy by distributing Na atoms across both the Na(1) and the Na(2) sites as compared to the configurational entropy that can be obtained from only within Na(2) sites (a full occupation of Na in Na(1) sites gives rise to a net zero configurational entropy from the Na(1) sites). Indeed, recent work on oxide perovskites has shown that configurational entropy on two different "sub-lattices" can often lead to higher entropy gain compared to a single sub-lattice.[48]

The configurational entropy $S(x)$ *vs.* Na content ($1 \leq x \leq 3$) at different temperatures is shown in Fig. S7 of ESI.† $S(x)$ shows a local minimum at $x = 1$, 2, and 3, in agreement with the single-phases observed in the phase diagram (Fig. 2). The low Na off-stoichiometry, up to temperatures as high as ~500 K at $x = 1$ and $x = 2$, reflects a trivial gain in configurational entropy with Na off-stoichiometry, available to these systems, as shown in Fig. S7.† Although we observe sizeable values of configurational entropy computed at high temperatures (above ~800 K) in the single-phase regions (ζ, ψ, and ω), these phases are still preserved and full "compositional" disorder is only achieved above ~900 K.

It is surprising that the metastable $N_{1.5}VP$ ordering (~4.4 meV f.u.$^{-1}$ above convex hull at 0 K, Fig. 1(b)) does not appear as a stable ordering at any temperature in our phase diagram (Fig. 2), while the metastable $N_{3.5}VP$ ordering (~8.0 meV f.u.$^{-1}$ above convex hull) becomes stable at ~10 K. While the energy above the convex hull is usually a good rule of thumb to estimate (*meta*)stability of phases, the important factor is which other phases are in competition with the (*meta*)stable phase of interest and their entropies.[49–51] In the case of $N_{1.5}VP$, the primary competing phase is N_2VP (the other competing phase is N_1VP), which remains a stable, stoichiometric compound up to ~480 K. Importantly, both $N_{1.5}VP$ and N_2VP orderings have their Na(1) sites fully occupied by Na, while 0.5 and 1 Na(2) sites per f.u. are occupied by Na, respectively (Fig. 3). Given that there are a maximum of three Na(2) sites per f.u., the N_2VP ordering can exhibit higher configurational entropy (corresponding to a Na occupancy of 0.33 in the Na(2) sites and assuming an ideal-solution-like behaviour), compared to the $N_{1.5}VP$ ordering (0.16 Na occupancy), resulting in N_2VP remaining stable relative to $N_{1.5}VP$ with increasing temperature and preventing the $N_{1.5}VP$ phase from appearing on the phase diagram. On the other hand, the primary phase that $N_{3.5}VP$ competes with is N_3VP (the other phase is N_4VP), which should exhibit lower configurational entropy than $N_{3.5}VP$, given that N_3VP exhibits an electrostatically-driven monoclinic distortion. This allows the stabilization of the $N_{3.5}VP$ ordering at low temperatures, albeit its higher energy above the convex hull.

The computed N_xVP voltage – composition curves at 0 K, 10 K, 300 K, and 500 K compared with the experimental voltage – composition data recorded at 298 K (ref. 21) are shown in Fig. 4. The blue (10 K), aqua (300 K) and gold (500 K) voltage profiles

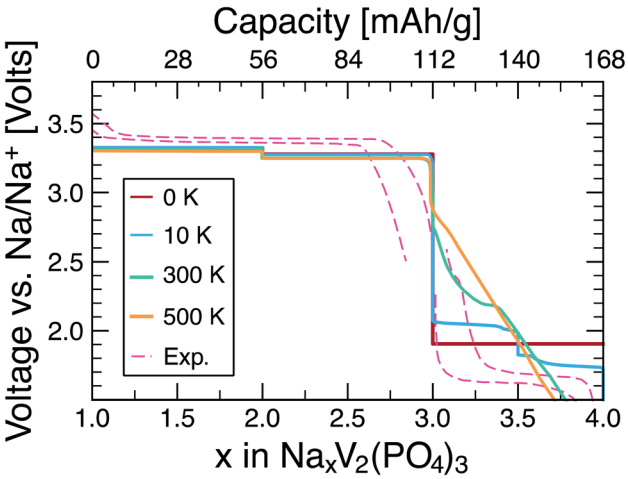

Fig. 4 Computed intercalation voltage (volts *vs.* Na/Na^+) curves as a function of Na content (x) in N_xVP. The pink dashed lines indicate the experimental voltage response of N_xVP at room temperature (digitized from ref. 21 for $3 \leq x \leq 4$). Notably, the experimental profile for $1 \leq x \leq 3$ is obtained from the unpublished works of some of the authors. The crimson line shows the computed voltage curve at 0 K derived by the DFT results from Fig. 1(b). The blue, aqua and gold lines display the computed voltage curves at 10 K, 300 K and 500 K, respectively, generated by the gcMC results. The discharge capacities (top x-axis in the unit of mA h g^{-1}) are normalized to N_4VP.

are obtained from gcMC simulations, and the crimson profile is obtained directly from DFT calculations (see eqn (S6) of the ESI†) at 0 K. Notably, the 0 K profile shows two voltage steps, corresponding to ψ and ω single phases, and consequently three voltage plateaus, corresponding to $\zeta + \psi$ (~3.29 V *vs.* Na/Na^+), $\psi + \omega$ (~3.24 V), and $\omega + \sigma$ (~1.89 V) two-phase regions. Generally, the computed voltage profiles at 0 K are in agreement with previous reports.[12,34,52,53]

Apart from a small (~50 mV) previously unreported voltage step at $x = 2$ (N_2VP), the voltage profiles for $1 \leq x \leq 3$ at different temperatures display a similar shape. Although there is good qualitative agreement between theory and experiment for the entire Na composition range, all the predicted voltage curves at the selected temperatures underestimate the average voltage across $1 \leq x \leq 3$, and overestimate the average voltage in the $3 \leq x \leq 4$ range compared to experiment.[21] Notably, the voltage curve in $3 \leq x \leq 4$ at 10 K shows a step at $x = 3.5$, which corresponds to the formation of θ phase *via* the eutectoid reaction shown in Fig. 2. At higher temperatures (300 K and 500 K), the voltage profile for $3 \leq x \leq 4$ region exhibits a sloping feature, characteristic of the predicted single phase domain (ω/θ/σ) at such temperatures (Fig. 2).

Discussion and conclusions

In this paper, we have investigated the thermodynamics of Na (de)intercalation in the NaSICON electrode material, $Na_3V_2(PO_4)_3$, for Na-ion batteries. Specifically, we derived the temperature-composition phase diagram of the N_xVP system and the temperature dependent voltage curves for the reversible (de)intercalation of Na-ions. Notably, we have identified

a previously uncharted, thermodynamically stable phase with composition N_2VP, and another metastable ordering at $N_{3.5}VP$. The existence of the N_2VP phase between N_1VP and N_3VP has been simultaneously confirmed by recent *operando* measurements.[36] In addition, we have studied other important properties, such as, the phase diagram at 0 K, the Na/vacancy and charge-ordered V configurations of the 0 K ground states, and the evolution of Na(1) and Na(2) occupancies with temperature and Na content. The following paragraphs contain additional observations from the data presented in this work as well as suggestions for future work.

Unarguably, DFT-based simulations of highly correlated systems, such as N_xVP (and other Na metal phosphates), present significant theoretical and computational challenges, which explain the scarce studies of such phase diagrams. Knowledge of compositional phase diagrams is however very important to accurately chart the electrochemical properties of these complex frameworks. Importantly, this is the first instance to report the composition *vs.* temperature phase diagram and temperature dependent voltage curves for NaSICON electrode N_xVP.

Three important observations can be made from the sodium occupancy data of the N_xVP system: (i) The Na(1) site does not appear electrochemically active at room temperature (and below), for $1 \leq x \leq 3$, which indicates that the Na^+ (de)intercalation is mostly driven by the Na(2) sites; (ii) at higher temperatures (>470 K) and higher Na contents ($x > 3$), both Na(1) and Na(2) attain nearly the same fractional occupations, which clearly indicates that the Na(1) site is indeed electrochemically active in these circumstances; and (iii) at $x = 1$, all Na(2) sites are empty and further Na removal will require the extraction of Na from Na(1) sites. With respect to observations (i) and (ii), we suggest that, at high temperature and x, Na^+ will be transferred between Na(1) and Na(2), which might kinetically facilitate the reversible Na (de)intercalation (at least for $x > 3$). Also, we expect that any electronic entropy arising from charge disordering on the vanadium sites in $1 \leq x \leq 3$ will promote disordering among the Na(1) and Na(2) sites. For observation (iii), we note that in 1992, Gopalakrishnan claimed chemical extraction of the last Na^+ from N_1VP,[54] but this result has not been yet successfully reproduced.[11–13,39] Our data indicates that, at $x = 1$, all Na ions only occupy Na(1) sites, and their extraction may affect the structural integrity of N_1VP, thus suppressing the chemical or electrochemical extraction of the last Na^+. Indeed, Na migration between Na(1) sites at N_1VP is hindered by high migration barriers (~755 meV, computed previously),[52] which usually indicate highly stable arrangement of atoms. Furthermore, the thermodynamic instability of the $V_2(PO_4)_3$ framework with respect decomposition into $VPO_5 + VP_2O_7$ can also account for the lack of reproduceable extraction of the last Na^+ from N_1VP.[12]

Previously, Na ion migration has been investigated in a number of N_xVP compositions. Huang *et al.* and Ishado *et al.* independently used nudged elastic band calculations to estimate Na migration barriers between Na(1) and Na(2) sites (~420 meV, and ~304 meV, respectively) in N_3VP, which suggest facile Na mobility in N_3VP as opposed to Na migration in N_1VP (~755 meV).[52,55]

During the construction of the N_xVP phase diagram, we isolated two novel low-temperature stable Na/vacancy orderings at the compositions N_2VP and $N_{3.5}VP$. Other low energy structures are visible from an analysis of the convex hull of Fig. 1, for example $N_{1.5}VP$ and $N_{3.25}VP$, but their structures are not stabilized by configurational entropy at increasing temperatures (see Fig. 2). Notably, the signature of N_2VP has been reported through *operando* X-ray diffraction by Zakharkin *et al.*,[35] but its structural features were never identified and reported. In addition, our gcMC predicts a new stable phase, $N_{3.5}VP$, that exists as the θ phase from 10 to ~120 K, after which it merges with the ω and σ phases into a larger monophasic region (Fig. 2).

The ground state triclinic structure of N_2VP (Fig. 2 and 4), which exists as a line compound from 0 K to ~480 K, displays a specific Na/vacancy ordering at low temperatures. At the structural level, the N_2VP ordering is achieved by the cooperative organization of the highly mobile Na-ions (occupying Na(2) sites) near V(III) sites and away from more positive V(IV) sites. The stability of the stoichiometric N_2VP ordering (*i.e.*, the solubility of excess Na or Na-vacancies) also depends upon the adaptability of the vanadium oxidation states by inter-valence electron transfer, which can be quantified by the impact of electronic entropy on the phase boundary of the ψ phase. Notably, we find that the inclusion of electronic entropy in our model only marginally modifies the N_xVP phase boundaries (Fig. 2), in contrast to other phosphate electrode materials (*e.g.*, $LiFePO_4$), where electron–hole localization affects the features of the phase diagram significantly.[56] Thus, we can conclude that charge ordering on the vanadium sites (as shown in Fig. 5) is more likely to drive specific Na/vacancy arrangements, especially at low temperatures. Since Na ions are expected to be highly mobile in NaSICON structures (as indicated in Fig. 5),[10] the disorder in the Na/vacancy sites is the main contributor to the configurational entropy of the ψ phase at higher temperatures and not any charge-disorder on the V sites, thus restricting the extent of Na off-stoichiometry exhibited by the ψ phase up to $T \sim 480$ K.

There are several reasons why N_2VP might be difficult to be observed in practice. First, we speculate that N_2VP might be difficult to isolate upon electrochemical (de)intercalation of Na. For example, the voltage step corresponding to N_2VP formation (~50 mV at $x = 2$ in Fig. 4) is similar to the magnitude of polarization that is typically observed in experiments. Standard electrochemical measurements may "bypass" the voltage signature of the stable N_2VP ordering. Second, N_2VP is only marginally stable with respect to disproportionation into N_1VP and N_3VP, as can be seen from Fig. 1(b) and 4, which may increase the difficulty of a direct solid-state synthesis of N_2VP from other precursors. Third, it may be simply too difficult to recognize the monoclinic or triclinic ($C2/c$ or $P\bar{1}$ according to our DFT relaxations) distorted N_2VP structures in the presence of the dominant rhombohedral N_1VP and/or N_3VP phases. In this context, specialized synthesis routes and/or "*operando*" experiments can be carried out to verify the existence of the

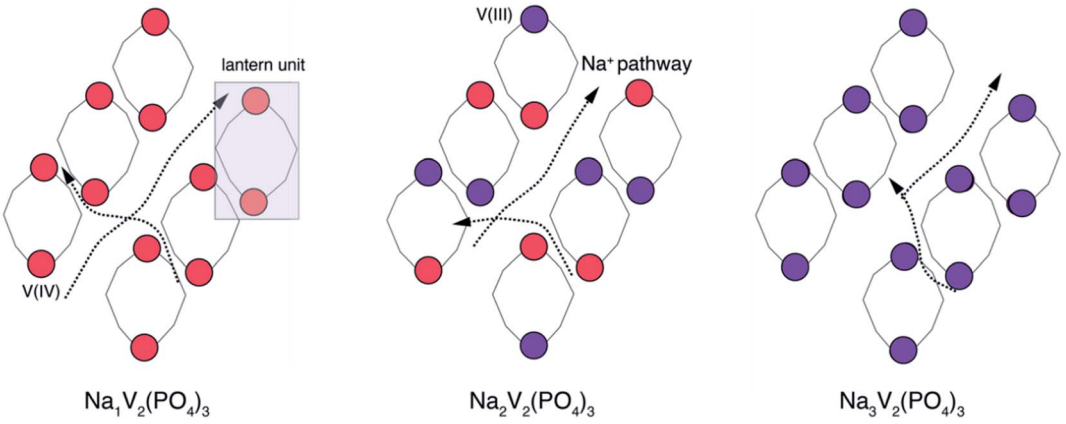

Fig. 5 Two-dimensional schematic of V charge orderings at different ground states, namely N_1VP, N_2VP and N_3VP. V(IV) and V(III) sites are represented by red and purple circles, respectively. The typical "lantern unit" is highlighted by the violet box. Na-ion pathways are shown with dashed arrow lines. The 3D arrangement of the "lantern" is not conveyed by this cartoon.

N_2VP ordering, similar to recent efforts that have been undertaken. Previous computational studies, with different exchange-correlation functionals, had indeed assigned N_2VP as a slightly metastable phase (~2 meV per atom above the convex hull), which might give an indication of the error bar in our computed data.[12]

The experimental voltage curve of Fig. 4 in the region $3 \leq x \leq 3.5$ shows an appreciable sloping behaviour followed by a voltage-composition plateau in the $3.5 \leq x \leq 4$ region, which is partially captured in our calculated voltage profiles at 300 K or 500 K.[21] It is not clear whether this sloping region is due to polarization effects (during either charging or discharging) encountered in the experiment, or due to solid solution behaviour, as evidenced by our predictions in Fig. 2 and 4. It also appears that the experiment could not achieve full Na insertion to reach N_4VP, which may be facilitated by higher temperature experiments, and requires further theoretical and experimental investigations.

The emergence of the intermediate N_2VP phase questions the accepted two-phase reaction between N_3VP and N_1VP, and calls for deeper investigations of the complex electrochemical behaviour of the N_xVP system and potentially other NaSICON electrodes. Our current understanding of the phase behaviour suggests that during charging (and discharging), particles of N_xVP will simultaneously contain domains with high (N_3VP) and low (N_1VP) levels of sodium content. The lattice mismatch between N_3VP and N_1VP domains can give rise to interfacial regions with significant strain (~6% volumetric strain, see Table S2†), which may affect the particle integrity, especially when cycled at a high-rate and/or over numerous cycles.[57] Our computed phase diagram and recent *operando* experiments[36] have revealed the presence and thermodynamic stability of the N_2VP phase. Importantly, N_2VP can act as a "bridge" phase between high-Na N_3VP and low-Na N_1VP phases, reducing the lattice mismatch between the N_3VP and N_1VP phases, eventually lowering the interfacial strain and enabling high-rate and/or sustained cycle life upon reversible Na intercalation in N_xVP.

Note that unearthing the thermodynamically stable phases in an electrode material has had significant impact on battery design and development in the past.[56] For example, understanding the phase behaviour of Li_xFePO_4 has enabled the optimization of rate-performance of this cathode material.[58] Thermodynamically, Li_xFePO_4 ($0 \leq x \leq 1$) should follow a two-phase reaction during Li (de)intercalation, where each Li_xFePO_4 cathode particle is split into Li-rich and Li-poor domains. However, when nano-sized, Li_xFePO_4 can access several transient phases, as confirmed by experimental studies,[59–65] which enable its high-rate performance. Similar sizing-effects may be explored for the optimization of the rate performance and cycle behavior in N_xVP, for which our work will act as a guide.

Methodology

To assess the structural, thermodynamic and electronic properties of N_xVP, we used the Vienna *ab initio* simulation package (VASP 6.1.0),[66,67] which implements density functional theory (DFT) to solve the Schrödinger equation of many-electron systems. The projector augmented wave (PAW) potentials, specifically Na 08Apr2002 $3s^1$, V_pv 07Sep2000 $3p^6 3d^4 4s^1$, P 06Sep2000 $2s^2 3p^3$, O 08Apr2002 $2s^2 2p^4$, were used for the description of the core electrons.[68] The valence electrons were expanded in terms of orthonormal plane-waves up to an energy cutoff of 520 eV.

To describe the electronic exchange-correlation, we employed the strongly constrained and appropriately normed (SCAN) *meta*-generalized gradient approximation (*meta*-GGA) functional.[40] SCAN includes the kinetic energy density contributions, which has been shown to remove the O_2 overbinding problem of GGA, while providing statistically-better ground-state electronic structures.[42] We also added a Hubbard U correction of 1.0 eV on all vanadium atoms to improve the localization of 3d electrons (*i.e.*, SCAN + U), and thus reduce the spurious electron self-interaction error.[42] In contrast to typical GGA + U calculations, a smaller U value is required for SCAN calculations, whose construction limits the self-interaction

error.[41,42,69] All our DFT calculations were spin-polarized and we initialized all structures in a ferromagnetic arrangement. The total energy of each calculation was converged to within 10^{-5} eV per cell, atomic forces within 10^{-2} eV Å^{-1} and the stress within 0.29 GPa.

To explore a sufficiently large number of Na/vacancy configurations in N_xVP, which is required to parameterize a cluster expansion (CE) model (see Section S2 in ESI†), we enumerated all the symmetrically distinct orderings in supercells containing as many as 8 f.u. (168 atoms) and with a resolution on the composition axis of $\Delta x = 0.25$. The enumeration process was performed with the pymatgen package.[70] At each composition, we chose a maximum of 500 structures with the lowest Ewald energy,[71] based on point charges (Na = +1, V = +2.5, P = +5, O = −2), to keep our calculations computationally tractable, followed by selecting only a subset of symmetrically distinct structures. In total, we have performed DFT structure relaxations (*i.e.*, relax the cell volume, cell shape, and ionic positions) for 849 structures, across $1 \leq x \leq 4$ in N_xVP, which formed our training set for the cluster expansion. The DFT total energy of the Na/vacancy orderings was integrated on a 3 × 3 × 3 Γ-centered Monkhorst–Pack[72] *k*-point mesh for all primitive structures containing 2 N_xVP formula units (f.u.), 42 atoms, a 1 × 3 × 3 *k*-point mesh applied to all supercells with 4 f.u. (84 atoms), and a 1 × 1 × 3 mesh in 8 f.u. (168 atoms), respectively.

Conflicts of interest

There are no conflicts to declare.

Acknowledgements

P. C., C. M., A. K. C., and J.-N. C. are grateful to the ANR-NRF NRF2019-NRF-ANR073 Na-MASTER. P.C. acknowledges funding from the National Research Foundation under his NRF Fellowship NRFF12-2020-0012. L. C., D. C. and C. M. acknowledge the ANRT and TIAMAT for the funding of S. P.'s PhD thesis as well as the financial support from the Région Nouvelle Aquitaine and from the French National Research Agency (STORE-EX Labex Project ANR-10-LABX-76-01). The computational work was performed using resources of the National Supercomputing Centre, Singapore (https://www.nscc.sg).

References

1 J. B. Goodenough and K.-S. Park, *J. Am. Chem. Soc.*, 2013, **135**, 1167–1176.
2 E. A. Olivetti, G. Ceder, G. G. Gaustad and X. Fu, *Joule*, 2017, **1**, 229–243.
3 J.-M. Tarascon, *Nature Chem*, 2010, **2**, 510.
4 S.-W. Kim, D.-H. Seo, X. Ma, G. Ceder and K. Kang, *Adv. Energy Mater.*, 2012, **2**, 710–721.
5 V. Palomares, P. Serras, I. Villaluenga, K. B. Hueso, J. Carretero-González and T. Rojo, *Energy Environ. Sci.*, 2012, **5**, 5884.
6 N. Yabuuchi, K. Kubota, M. Dahbi and S. Komaba, *Chem. Rev.*, 2014, **114**, 11636–11682.
7 J. L. Kaufman, J. Vinckevičiūtė, S. Krishna Kolli, J. Gabriel Goiri and A. Van der Ven, *Phil. Trans. R. Soc. A.*, 2019, **377**, 20190020.
8 R. Usiskin, Y. Lu, J. Popovic, M. Law, P. Balaya, Y.-S. Hu and J. Maier, *Nat. Rev. Mater.*, 2021, **6**, 1020–1035.
9 H. Y.-P. Hong, *Mater. Res. Bull.*, 1976, **11**, 173–182.
10 J. B. Goodenough, H. Y.-P. Hong and J. A. Kafalas, *Mater. Res. Bull.*, 1976, **11**, 203–220.
11 C. Masquelier and L. Croguennec, *Chem. Rev.*, 2013, **113**, 6552–6591.
12 B. Singh, Z. Wang, S. Park, G. S. Gautam, J.-N. Chotard, L. Croguennec, D. Carlier, A. K. Cheetham, C. Masquelier and P. Canepa, *J. Mater. Chem. A*, 2021, **9**, 281–292.
13 T. Jin, H. Li, K. Zhu, P.-F. Wang, P. Liu and L. Jiao, *Chem. Soc. Rev.*, 2020, **49**, 2342–2377.
14 N. Tapia-Ruiz, A. R. Armstrong, H. Alptekin, M. A. Amores, H. Au, J. Barker, R. Boston, W. R. Brant, J. M. Brittain, Y. Chen, M. Chhowalla, Y.-S. Choi, S. I. R. Costa, M. Crespo Ribadeneyra, S. A. Cussen, E. J. Cussen, W. I. F. David, A. V. Desai, S. A. M. Dickson, E. I. Eweka, J. D. Forero-Saboya, C. P. Grey, J. M. Griffin, P. Gross, X. Hua, J. T. S. Irvine, P. Johansson, M. O. Jones, M. Karlsmo, E. Kendrick, E. Kim, O. V. Kolosov, Z. Li, S. F. L. Mertens, R. Mogensen, L. Monconduit, R. E. Morris, A. J. Naylor, S. Nikman, C. A. O'Keefe, D. M. C. Ould, R. G. Palgrave, P. Poizot, A. Ponrouch, S. Renault, E. M. Reynolds, A. Rudola, R. Sayers, D. O. Scanlon, S. Sen, V. R. Seymour, B. Silván, M. T. Sougrati, L. Stievano, G. S. Stone, C. I. Thomas, M.-M. Titirici, J. Tong, T. J. Wood, D. S. Wright and R. Younesi, *J. Phys. Energy*, 2021, **3**, 031503.
15 A. Ponrouch, E. Marchante, M. Courty, J.-M. Tarascon and M. R. Palacín, *Energy Environ. Sci.*, 2012, **5**, 8572.
16 P. G. Kitz, M. J. Lacey, P. Novák and E. J. Berg, *Anal. Chem.*, 2019, **91**, 2296–2303.
17 *Na-ion Batteries*, ed. L. Monconduit and L. Croguennec, ISTE Ltd/John Wiley and Sons Inc, Hoboken, 2020.
18 V. Lacivita, Y. Wang, S.-H. Bo and G. Ceder, *J. Mater. Chem. A*, 2019, **7**, 8144–8155.
19 Q. Ma, C.-L. Tsai, X.-K. Wei, M. Heggen, F. Tietz and J. T. S. Irvine, *J. Mater. Chem. A*, 2019, **7**, 7766–7776.
20 K. Saravanan, C. W. Mason, A. Rudola, K. H. Wong and P. Balaya, *Adv. Energy Mater.*, 2013, **3**, 444–450.
21 F. Lalère, V. Seznec, M. Courty, R. David, J. N. Chotard and C. Masquelier, *J. Mater. Chem. A*, 2015, **3**, 16198–16205.
22 F. Lalère, J. B. Leriche, M. Courty, S. Boulineau, V. Viallet, C. Masquelier and V. Seznec, *J. Power Sources*, 2014, **247**, 975–980.
23 T. Lan, Q. Ma, C. Tsai, F. Tietz and O. Guillon, *Batteries Supercaps*, 2021, **4**, 479–484.
24 C. Delmas, J. Braconnier, C. Fouassier and P. Hagenmuller, *Solid State Ionics*, 1981, **3–4**, 165–169.
25 A. J. Toumar, S. P. Ong, W. D. Richards, S. Dacek and G. Ceder, *Phys. Rev. Appl.*, 2015, **4**, 064002.
26 I. Hasa, S. Mariyappan, D. Saurel, P. Adelhelm, A. Y. Koposov, C. Masquelier, L. Croguennec and M. Casas-Cabanas, *J. Power Sources*, 2021, **482**, 228872.

27 Z. Deng, G. Sai Gautam, S. K. Kolli, J.-N. Chotard, A. K. Cheetham, C. Masquelier and P. Canepa, *Chem. Mater.*, 2020, **32**, 7908–7920.
28 S. Y. Lim, H. Kim, R. A. Shakoor, Y. Jung and J. W. Choi, *J. Electrochem. Soc.*, 2012, **159**, A1393–A1397.
29 H. Kabbour, D. Coillot, M. Colmont, C. Masquelier and O. Mentré, *J. Am. Chem. Soc.*, 2011, **133**, 11900–11903.
30 X. Yao, Z. Zhu, Q. Li, X. Wang, X. Xu, J. Meng, W. Ren, X. Zhang, Y. Huang and L. Mai, *ACS Appl. Mater. Interfaces*, 2018, **10**, 10022–10028.
31 J.-N. Chotard, G. Rousse, R. David, O. Mentré, M. Courty and C. Masquelier, *Chem. Mater.*, 2015, **27**, 5982–5987.
32 Z. Jian, C. Yuan, W. Han, X. Lu, L. Gu, X. Xi, Y.-S. Hu, H. Li, W. Chen, D. Chen, Y. Ikuhara and L. Chen, *Adv. Funct. Mater.*, 2014, **24**, 4265–4272.
33 Y. Ishado, A. Inoishi and S. Okada, *Electrochemistry*, 2020, **88**, 457–462.
34 Y. Noguchi, E. Kobayashi, L. S. Plashnitsa, S. Okada and J. Yamaki, *Electrochim. Acta*, 2013, **101**, 59–65.
35 M. V. Zakharkin, O. A. Drozhzhin, S. V. Ryazantsev, D. Chernyshov, M. A. Kirsanova, I. V. Mikheev, E. M. Pazhetnov, E. V. Antipov and K. J. Stevenson, *J. Power Sources*, 2020, **470**, 228231.
36 S. Park, Z. Wang, Z. Deng, I. Moog, P. Canepa, F. Fauth, D. Carlier, L. Croguennec, C. Masquelier and J.-N. Chotard, Crystal Structure of the Intermediate Na2V2(PO4)3 Phase and Electrochemical Reaction Mechanisms in NaxV2(PO4)3 ($1 \leq x \leq 4$) System, 2021, DOI: 10.33774/chemrxiv-2021-q6z1p.
37 J. M. Sanchez, F. Ducastelle and D. Gratias, *Phys. A*, 1984, **128**, 334–350.
38 A. Van der Ven, J. C. Thomas, Q. Xu and J. Bhattacharya, *Math. Comput. Simulat.*, 2010, **80**, 1393–1410.
39 J. C. Thomas and A. V. der Ven, *Phys. Rev. B: Condens. Matter Mater. Phys.*, 2013, **88**, 214111.
40 J. Sun, A. Ruzsinszky and J. P. Perdew, *Phys. Rev. Lett.*, 2015, **115**, 036402.
41 G. Sai Gautam and E. A. Carter, *Phys. Rev. Mater.*, 2018, **2**, 095401.
42 O. Y. Long, G. Sai Gautam and E. A. Carter, *Phys. Rev. Mater.*, 2020, **4**, 045401.
43 J. Feinleib and W. Paul, *Phys. Rev.*, 1967, **155**, 841–850.
44 C. Didier, M. Guignard, J. Darriet and C. Delmas, *Inorg. Chem.*, 2012, **51**, 11007–11016.
45 M. Guignard, C. Didier, J. Darriet, P. Bordet, E. Elkaïm and C. Delmas, *Nat. Mater.*, 2013, **12**, 74–80.
46 T. Holstein, *Ann. Phys.*, 1959, **8**, 325–342.
47 M. Reticcioli, U. Diebold, G. Kresse and C. Franchini, in *Handbook of Materials Modeling*, ed. W. Andreoni and S. Yip, Springer International Publishing, Cham, 2020, pp. 1035–1073.
48 G. Sai Gautam, E. B. Stechel and E. A. Carter, *Chem. Mater.*, 2020, **32**, 9964–9982.
49 W. Sun, S. T. Dacek, S. P. Ong, G. Hautier, A. Jain, W. D. Richards, A. C. Gamst, K. A. Persson and G. Ceder, *Sci. Adv.*, 2016, **2**, e1600225.
50 D. C. Hannah, G. Sai Gautam, P. Canepa and G. Ceder, *Adv. Energy Mater.*, 2018, **8**, 1800379.
51 D. De Fontaine, *Principles of Classical Thermodynamics: Applied to Materials Science*, World Scientific Publishing Co. Pte. Ltd, Singapore ; Hackensack, NJ, 2019.
52 Y. Ishado, A. Inoishi and S. Okada, *Electrochemistry*, 2020, **88**, 457–462.
53 X. Guo, Z. Wang, Z. Deng, B. Wang, X. Chen and S. P. Ong, *Chem. Mater.*, 2020, **32**, 6875–6885.
54 J. Gopalakrishnan and K. K. Rangan, *Chem. Mater.*, 1992, **4**, 745–747.
55 Y. Huang, X. Li, J. Wang, L. Miao, C. Li, J. Han and Y. Huang, *Energy Storage Materials*, 2018, **15**, 108–115.
56 F. Zhou, T. Maxisch and G. Ceder, *Phys. Rev. Lett.*, 2006, **97**, 155704.
57 A. Abdellahi, O. Akyildiz, R. Malik, K. Thornton and G. Ceder, *J. Mater. Chem. A*, 2014, **2**, 15437–15447.
58 R. Malik, A. Abdellahi and G. Ceder, *J. Electrochem. Soc.*, 2013, **160**, A3179–A3197.
59 C. Delacourt, J. Rodríguez-Carvajal, B. Schmitt, J.-M. Tarascon and C. Masquelier, *Solid State Sci.*, 2005, **7**, 1506–1516.
60 C. Delacourt, P. Poizot, J.-M. Tarascon and C. Masquelier, *Nat. Mater.*, 2005, **4**, 254–260.
61 R. G. Iyer, C. Delacourt, C. Masquelier, J.-M. Tarascon and A. Navrotsky, *Electrochem. Solid-State Lett.*, 2006, **9**, A46–A48.
62 L. Laffont, C. Delacourt, P. Gibot, M. Y. Wu, P. Kooyman, C. Masquelier and J. M. Tarascon, *Chem. Mater.*, 2006, **18**, 5520–5529.
63 Y. Orikasa, T. Maeda, Y. Koyama, H. Murayama, K. Fukuda, H. Tanida, H. Arai, E. Matsubara, Y. Uchimoto and Z. Ogumi, *Chem. Mater.*, 2013, **25**, 1032–1039.
64 I. Takahashi, T. Mori, T. Yoshinari, Y. Orikasa, Y. Koyama, H. Murayama, K. Fukuda, M. Hatano, H. Arai, Y. Uchimoto and T. Terai, *J. Power Sources*, 2016, **309**, 122–126.
65 T. Yoshinari, T. Mori, K. Otani, T. Munesada, K. Yamamoto, T. Uchiyama, K. Fukuda, Y. Koyama, R. Hagiwara, Y. Orikasa and Y. Uchimoto, *Chem. Mater.*, 2019, **31**, 7160–7166.
66 G. Kresse and J. Furthmüller, *Comput. Mater. Sci.*, 1996, **6**, 15–50.
67 G. Kresse and J. Furthmüller, *Phys. Rev. B: Condens. Matter Mater. Phys.*, 1996, **54**, 11169–11186.
68 G. Kresse and D. Joubert, *Phys. Rev. B: Condens. Matter Mater. Phys.*, 1999, **59**, 1758–1775.
69 D. A. Kitchaev, H. Peng, Y. Liu, J. Sun, J. P. Perdew and G. Ceder, *Phys. Rev. B*, 2016, **93**, 045132.
70 S. P. Ong, W. D. Richards, A. Jain, G. Hautier, M. Kocher, S. Cholia, D. Gunter, V. L. Chevrier, K. A. Persson and G. Ceder, *Comput. Mater. Sci.*, 2013, **68**, 314–319.
71 P. P. Ewald, *Ann. Phys.*, 1921, **369**, 253–287.
72 J. D. Pack and H. J. Monkhorst, *Phys. Rev. B: Solid State*, 1977, **16**, 1748–1749.